

1  
2  
3  
4  
5  
6  
7  
8  
9  
10  
11  
12  
13  
14  
15  
16  
17  
18

## REVISION 1

**TITLE:** Experimental observations of TiO<sub>2</sub> activity in rutile-undersaturated melts

**AUTHORS:** Michael R. Ackerson, Bjørn O. Mysen

### ABSTRACT

An estimate of TiO<sub>2</sub> activity ( $a_{\text{TiO}_2}^{\text{melt-sat.}}$ ) is necessary for the application of trace-element thermobarometry of magmatic systems where melts are typically under-saturated with respect to rutile/anatase. Experiments were performed in the system SiO<sub>2</sub>-Na<sub>2</sub>O-TiO<sub>2</sub> to develop two independent methods of estimating  $a_{\text{TiO}_2}^{\text{melt-sat.}}$ — one based on the commonly applied rutile-saturation technique and another utilizing a novel Ti-in-tridymite thermometer. It is demonstrated that the rutile-saturation model can lead to an overestimate of  $a_{\text{TiO}_2}^{\text{melt-sat.}}$  relative to TiO<sub>2</sub> activity calculated using the solubility of Ti in tridymite (SiO<sub>2</sub>) coexisting with rutile. Overestimation via the rutile-saturation technique is due to variations in the solubility mechanisms of Ti in the melt phase as a function of Ti content. In natural systems, overestimates of  $a_{\text{TiO}_2}^{\text{melt-sat.}}$  will lead to an underestimation of crystallization temperatures by Ti-based trace-element thermobarometers. Although this study is not directly applicable to natural systems, it lays the groundwork for future research on natural composition magmas to constrain TiO<sub>2</sub> activity in melts.

### INTRODUCTION

Over the past decade, trace-element thermobarometry has emerged as a powerful tool to determine the thermal and barometric histories of igneous and metamorphic rocks. The thermodynamic basis for trace-element thermobarometry requires constraints on the activities of the chemical species

22 involved in the reactions that define the thermobarometers. For example, the Ti-in-quartz  
23 thermobarometer (Thomas et al. 2010) is based on the reaction  $TiO_2^{rutile} = TiO_2^{quartz}$ . Given an  
24 equilibrium constant  $K_{eq} \approx \frac{a_{TiO_2}^{quartz}}{a_{TiO_2}^{rutile}}$  ( $a_x^i$  is the activity of component x in phase i) and by  
25 assuming the low concentration of  $TiO_2$  in quartz is within the Henry's Law region such that  $a_{TiO_2}^{quartz} =$   
26  $kX_{TiO_2}^{quartz}$  (where  $k$  is a Henry's Law constant and  $X$  is the mol fraction of  $TiO_2$  in quartz) and rutile is  
27 nearly pure ( $a_{TiO_2}^{rutile} \approx 1$ ), the equilibrium Gibbs free energy expression provides a functional form  
28 through which experimental data can be fit to arrive at the experimentally-calibrated expression:

$$29 \quad RT \ln X_{TiO_2}^{quartz} = -60952 + 1.520T - 1741P + RT \ln a_{TiO_2}^{melt-sat.} \quad (1)$$

30 that relates the amount of Ti in quartz to temperature, pressure, and the  $a_{TiO_2}^{melt-sat.}$  (see Wark and Watson  
31 2006; Ferry and Watson 2007; Ghiorso and Gualda 2013; Hofmann et al. 2013 for further discussion).

32 In expression (1),  $a_{TiO_2}^{melt-sat.}$  is  $TiO_2$  activity expressed relative to rutile saturation in the melt as  
33 opposed to  $a_{TiO_2} = 1$  when the system is pure  $TiO_2$ . Practically, this means that in a silicate melt at rutile  
34 saturation, adding more titania to the melt will result in the crystallization of an equimolar quantity of  
35 rutile within the system while the  $TiO_2$  content of the melt remains constant. So, in the presence of rutile,  
36 this melt is saturated in  $TiO_2$  (Ghiorso and Gualda 2013). When rutile and quartz grow in  
37 equilibrium,  $a_{TiO_2}^{melt-sat.} = 1$ . However, most quartz- and zircon-bearing igneous and metamorphic rocks  
38 do not contain rutile, in which case the system is undersaturated relative to  $TiO_2$  ( $a_{TiO_2}^{melt-sat.} < 1$ ) and  
39  $a_{TiO_2}^{melt-sat.}$  must be estimated by other means.

40 In rutile-undersaturated systems,  $a_{TiO_2}^{melt-sat.}$  needs to be estimated by independent means in order  
41 to apply Ti-based trace-element thermobarometers. A number of different methods have been proposed to  
42 estimate  $a_{TiO_2}^{melt-sat.}$  in rutile-undersaturated systems. These include rutile-saturation modelling that relies

43 on the assumption that there is a linear relationship (Henry's Law behavior) between  $a_{\text{TiO}_2}^{\text{melt-sat.}}$  and the  
44 amount of  $\text{TiO}_2$  ( $X_{\text{TiO}_2}^{\text{melt}}$ ) dissolved in the melt (Hayden and Watson 2007; Gaetani et al. 2008; Shane et al.  
45 2008; Kularatne and Audéat 2014), compositions of co-crystallizing cubic and rhombohedral iron-  
46 titanium oxides (Wark et al. 2007; Ghiorso and Gualda 2013), MELTS and rhyolite-MELTS calculations  
47 (Thomas and Watson 2012; Kularatne and Audéat 2014), or by assuming that  $a_{\text{TiO}_2}^{\text{melt-sat.}}$  is buffered by  
48 the presence of titanium-rich mineral phases (e.g., titanite and ilmenite, Wark and Watson 2006; Thomas  
49 et al. 2010).

50 In many cases, utilizing multiple techniques to estimate  $a_{\text{TiO}_2}^{\text{melt-sat.}}$  can result in a range of values  
51 for  $a_{\text{TiO}_2}^{\text{melt-sat.}}$ . For example,  $a_{\text{TiO}_2}^{\text{melt-sat.}}$  estimates for the Bishop Tuff range from  $\sim 0.15$  by using MELTS  
52 to characterize melt inclusions (Thomas and Watson 2012) to  $\sim 0.69$  from equilibrium between  
53 rhombohedral and cubic iron-titanium oxides (Ghiorso and Gualda 2013). The value from rutile-  
54 saturation model estimates falls in the middle ( $\sim 0.55$ ). At 200 MPa and 100 ppm Ti in quartz, this range  
55 of  $a_{\text{TiO}_2}^{\text{melt-sat.}}$  yields temperature estimates between  $\sim 608$  and  $793$  °C. This discrepancy highlights the  
56 need for novel mechanisms to estimate  $a_{\text{TiO}_2}^{\text{melt-sat.}}$  in natural magmatic systems.

57 An understanding of possible reasons for the apparent variations in  $a_{\text{TiO}_2}^{\text{melt-sat.}}$  estimates and a  
58 mechanism by which to accurately predict  $a_{\text{TiO}_2}^{\text{melt-sat.}}$  is critical to the application of Ti-based trace-  
59 element thermobarometers. For example, measuring the Ti content of quartz crystallized experimentally  
60 in rhyolite bulk compositions at known T and P and various degrees of rutile-undersaturation could be  
61 used as a direct probe of  $a_{\text{TiO}_2}^{\text{melt-sat.}}$  that could be applied directly to natural quartz-glass pairs (e.g., melt  
62 inclusions in quartz). This would require an experimental approach that can crystallize quartz large  
63 enough to analyze from rhyolitic composition melts. However, experimental limitations have thus far  
64 hindered a direct experimental approach. It is extremely difficult to grow either quartz or zircon in Si-rich  
65 compositions to sizes large enough to analyze for Ti content. This fact has led researchers performing

66 experimentally-calibrated trace-element thermobarometers to employ hydrous fluids as a crystallization  
67 media in lieu of silicate melts (Watson and Harrison 2005; Thomas et al. 2010; Huang and Audétat 2012).  
68 In all of these experimental systems, there is no silicate melt phases, making it impossible to study  
69 composition-activity relations at rutile-undersaturation that can be directly applied to natural magmas.

70 Because of the limitations of using natural compositions, we employ Na-silicate compositions for  
71 this study, which have been used as model compounds for natural Si-rich magmas for decades (Zotov and  
72 Keppler 1998; Cody et al. 2005; Roskosz et al. 2006; Mysen 2011). In this compositional field, tridymite  
73 and rutile can be crystallized in equilibrium with a silicate melt. Although the results from this system are  
74 not directly applicable to natural systems, they lay the groundwork for understanding potential variations  
75 in  $a_{\text{TiO}_2}^{\text{melt-sat.}}$  estimates in nature. In this study, we will utilize two methods (a rutile-saturation model and  
76 a Ti-in-tridymite solubility calibration) to calculate  $a_{\text{TiO}_2}^{\text{melt-sat.}}$  in rutile-undersaturated synthetic glasses.  
77 Together with Raman investigation of the structure of Ti-bearing synthetic glasses we will discuss  
78 potential mechanisms by which different techniques can result in disparate estimates of  $a_{\text{TiO}_2}^{\text{melt-sat.}}$  and  
79 provide a potential framework for future experiments on natural composition melts to understand the  
80 causes of disparate estimates of  $a_{\text{TiO}_2}^{\text{melt-sat.}}$ .

## 81 **METHODS**

82 All experiments utilized powdered synthetic glass starting materials. Glasses were synthesized  
83 from thoroughly mixed SiO<sub>2</sub>, Na<sub>2</sub>CO<sub>3</sub> and TiO<sub>2</sub> powders by heating first at ~100 °C/hr from 700-900 °C  
84 to convert Na<sub>2</sub>CO<sub>3</sub> to Na<sub>2</sub>O, and then at 150 °C/hr to ~50-100 °C above their liquidus. The samples were  
85 then held at this temperature for 1 hour. The melts were quenched to glass by removing from the furnace  
86 and allowing to cool rapidly in air. Quenched glasses were powdered in an agate pestle and mortar under  
87 ethanol for ~1 hour to achieve a glass powder with a <30 μm average grain size.

88 Powdered glass starting material was loaded into ~5 mm diameter, 8 mm long platinum crucibles  
89 and placed in a Deltech 1-atm vertical tube furnace at their experimental temperatures for at least 24  
90 hours. Experiments were quenched by removing the crucibles from the furnace and lightly placing the  
91 bottom of the crucible in a water bath to quench the material to glass at room temperature in less than 15  
92 seconds. Glasses were removed from the crucibles, after which crucibles were inspected for leaks by  
93 filling with ethanol to ensure no water incursion upon quench. Experiments were performed on bulk  
94 compositions along  $\text{Na}_2\text{O}\cdot 8\text{SiO}_2(\text{NS8})\text{-TiO}_2$  join with 0-20 mol %  $\text{TiO}_2$  (Fig. 1). We use the sample  
95 nomenclature  $\text{TiXNS8}$ , where X is the mol %  $\text{TiO}_2$  in the bulk composition. The system  $\text{SiO}_2\text{-Na}_2\text{O-TiO}_2$   
96 was chosen for several reasons. First, its chemical simplicity allows for more accurate interpretation of  
97 Raman spectra than would be possible in natural multicomponent compositions. This advantage makes it  
98 possible to interpret solution mechanisms that govern Ti incorporation in the melt via Raman  
99 spectroscopy. Secondly, initial experiments performed in haplogranitic bulk compositions were  
100 performed at lower temperatures due to quartz-out reactions occurring relatively close to the solidus  
101 temperature (Piwinskii 1973; Maaløe and Wyllie 1975; Johannes 1984). As such, quartz crystals in these  
102 experiments were too small for accurate electron microprobe analyses (typically  $< 1 \mu\text{m}$ ). In the system  
103  $\text{SiO}_2\text{-Na}_2\text{O-TiO}_2$ , tridymite is stable to higher temperatures, which enabled crystals to grow to 25-30  $\mu\text{m}$   
104 on average. This is sufficiently large to perform high-quality chemical analysis of the tridymite grains.

105 Both starting material and experimental run products were inspected optically and in immersion  
106 oils in polarized light to ensure the run products were glasses and to observe crystalline phases below the  
107 liquidus. All starting material glasses were transparent with no opalescence, suggesting no  
108 cryptocrystalline minerals were present in the synthetic glass starting material. No opalescence was  
109 observed in experimental run products either above or below the liquidus. Further, X-ray Diffraction  
110 (XRD) analyses were performed using a Rigaku D-MAX Rapid microdiffractometer with a  $\text{Mo K}\alpha$   
111 source and image plate detector to validate the mineral phases (e.g., rutile versus anatase) and to ensure  
112 no cryptocrystalline phases had been formed during the experiment or upon quench (Supplementary Fig.

113 S1). Whereas cryptocrystalline anatase has been observed in glasses along the TiO<sub>2</sub>-SiO<sub>2</sub> join (e.g.,  
114 Henderson and Fleet 1995), there is no indication of cryptocrystalline anatase in any of the glasses from  
115 this experimental setup along the NS8-TiO<sub>2</sub> join via optical or XRD techniques.

116 Electron Probe Microanalyzer (EPMA) and scanning electron microscope (SEM) analyses of Ti  
117 in tridymite measure consistently similar data (Supplementary Table ST1), whereas EPMA data on  
118 glasses consistently recorded lower Na content, likely due to Na loss due to the beam current being ~20x  
119 greater than the SEM. Because of the reproducibility of Ti in tridymite data between the two techniques  
120 and the potential for Na loss in the microprobe analyses, we use SEM data for discussion in this  
121 manuscript. It should be noted that even after being held for 24 hours at elevated temperature, SEM  
122 analyses of the Ti20NS8 glass indicate little to no Na loss from the glass (Supplementary Table ST2).

### 123 *Chemical Analyses*

124 Chemical analysis of the mineral and melt run products were conducted on the JEOL 6500F  
125 scanning electron microscope (SEM) at the Carnegie Institution of Washington. Quantitative EDS was  
126 performed using the Oxford X-Max SDD-EDS detector on the 6500F. EDS spectra were calibrated using  
127 a basalt glass standard following the technique outlined in Armstrong 2014. SEM analyses were  
128 performed using a 10 keV ~1 nA beam with 20 s acquisition times. Test analyses of tridymite and glasses  
129 were performed on the 8530F EPMA at the Carnegie Institution of Washington to validate the accuracy of  
130 the SEM analyses. EPMA analyses were performed using a 10 keV accelerating voltage and 20 nA  
131 current for 60 second counting times on tridymite and 30 s on glasses. For both SEM and EPMA analyses  
132 the electron beam diameter was defocused to 5 μm on tridymite and 20 μm on the glass in order to reduce  
133 Na loss from the glass. A linear time-dependent intensity correction was enacted for all elements on the  
134 microprobe to mitigate the effects of beam damage. EPMA standards were quartz, rutile and jadeite, for  
135 Si, Ti, and Na, respectively. Several tridymite crystals from Ti20NS8 experiments were also extracted  
136 from the glass, mounted individually in epoxy and analyzed in order to verify that secondary fluorescence

137 from the glass did not contribute to measured Ti concentrations in the tridymite. All data presented in the  
138 figures are from EDS measurements.

### 139 ***Raman Spectroscopy***

140 Raman spectra were collected with a Jasco NRS 3100 confocal Raman spectrometer. The system  
141 is equipped with a 490 nm solid-state laser for sample excitation with a laser power of 39.1 mW on the  
142 sample. Spectra were collected using a 1200 lines/mm grating, which results in  $3\text{ cm}^{-1}$  resolution. Spectra  
143 were collected for 40 s over two acquisitions. The spectra were background-corrected with a linear  
144 background subtraction from  $370\text{ cm}^{-1}$  to  $1260\text{ cm}^{-1}$ . At higher Ti concentrations, the Raman spectra at  
145 low wavenumbers were truncated by the notch filter, making it impractical to attempt curve fitting for this  
146 complex region. Furthermore, as the intensity of the low wavenumber peaks increased (region from  $\sim 300$ -  
147  $500\text{ cm}^{-1}$ ), it became impractical to reliably and systematically apply background corrections that would  
148 consistently subtract out these regions, as has been done for different Na-silicate glasses that exhibited  
149 smaller changes in this low wavenumber region (e.g., Henderson and Fleet 1995). For our purposes, a  
150 simple linear background subtraction was deemed the simplest and most effective way to observe changes  
151 in the glass structure as a function of bulk  $\text{TiO}_2$  content consistently across the sample suite. Above  $1260$   
152  $\text{cm}^{-1}$  spectral intensities were consistent between experiments, indicating that subtraction of backgrounds  
153 down to the notch filter is not artificially transforming the low wavenumber regions to higher intensities.

## 154 **RESULTS**

155 The upper temperature limit investigated was governed by the stability field of the phases of  
156 interest. For example the Ti20NS8 experiments were performed up to  $1325\text{ }^\circ\text{C}$ , above which samples  
157 were completely melted. Rutile and tridymite occurred as  $5\text{-}40\text{ }\mu\text{m}$  crystals in the quenched silicate  
158 glasses. No experiments below 20 mol %  $\text{TiO}_2$  contained rutile, and tridymite was the liquidus phase in  
159 all but the Ti20NS8 experiments (Fig. 2). In rutile-undersaturated experiments, melt compositions  
160 followed trends expected in the presence of tridymite crystallization— decreasing temperatures favored

161 increasing tridymite crystallization which in turn led to increasing  $\text{TiO}_2$  and  $\text{Na}_2\text{O}$  in the melt (Fig. 3,  
162 Table 1).  $\text{TiO}_2$  concentrations in tridymite ranged from 0.12 to a maximum of 1.75 wt. %  $\text{TiO}_2$  in the  
163 rutile-saturated Ti20NS8 glass at 1300 °C (Table 2). SEM measurements indicate that the Ti content of  
164 tridymite crystals increases with increasing temperature.

165 In Ti-free NS8 glass, Raman spectra contain peaks consistent with vibrational modes of Si  
166 tetrahedral networks, including peaks near  $1100\text{ cm}^{-1}$ ,  $800\text{ cm}^{-1}$  and  $\text{Q}^3\text{-Q}^3$  Si-O vibrational modes below  
167  $\sim 650\text{ cm}^{-1}$  (Bell et al. 1968; Sen and Thorpe 1977; McMillan 1984). Ti-bearing glasses have prominent  
168 Raman peaks grouped near  $\sim 900\text{ cm}^{-1}$ ,  $700\text{-}800\text{ cm}^{-1}$ , and below  $\sim 650\text{ cm}^{-1}$  (similar to those observed by  
169 Henderson and Fleet 1995). At low Ti concentrations (below 10 mol %  $\text{TiO}_2$ ) the peaks near  $900\text{ cm}^{-1}$   
170 dominate the Raman spectra, whereas the lower frequency peaks are dominant at higher Ti  
171 concentrations. For a given bulk composition, no significant differences were observed between the  
172 corrected spectra for super- and sub-liquidus glasses.

173 The average coordination of Ti in the melt ([4]-, [5]-, or [6]-fold) and the mechanisms by which  
174 Ti is incorporated (as a network-forming or network-modifying cation, or as isolated clusters of Ti) can  
175 qualitatively be assessed using Raman spectroscopy of the quenched synthetic glasses. Raman spectra of  
176 quenched glasses (Fig. 4) show evidence of significant changes to the structure of the Ti-bearing Na-  
177 silicate glasses as a function of Ti content. Overall, the total intensity of the Raman signal increases with  
178 increasing Ti content. The Ti-free NS8 glass contains Raman peaks at  $\sim 1100\text{ cm}^{-1}$  and  $\sim 1150\text{ cm}^{-1}$  that  
179 can be attributed to Si-O stretching of  $\text{Q}^3$  and  $\text{Q}^4$  speciation of Si in the melt, respectively (e.g., Le Losq et  
180 al. 2015). Peaks from  $300\text{-}500\text{ cm}^{-1}$  can be attributed to symmetrical stretching of Si-O-Si bonds (Seifert  
181 et al. 1983; Mcmillan et al. 1984) in silicate rings and the peak at  $\sim 800\text{ cm}^{-1}$  is attributed to oxygen  
182 vibrations (Mysen and Richet 2005).

183 At low  $\text{TiO}_2$  concentrations a set of peaks begins to emerge from  $\sim 880\text{-}1000\text{ cm}^{-1}$ . These peaks  
184 have been attributed to  $^{[4]}\text{Ti}$  as either a network-forming cation or as  $^{[5]}\text{Ti}$  clusters (Henderson and Fleet



185 1995; Mysen and Neuville 1995). The most intense of these peaks ( $\sim 900\text{ cm}^{-1}$ ) has also been attributed to  
186 stretching vibrations of  $^{[5]}\text{Ti}$  (Reynard and Webb 1998) in titanyl groups (Farges 1997). The intensity of  
187 this group of peaks continues to increase with increasing Ti content. Peaks that appear prominently  
188 between  $\sim 650\text{-}800\text{ cm}^{-1}$  in the spectra starting around 10 mol%  $\text{TiO}_2$  have been attributed to Ti in either  
189  $^{[4]}\text{Ti}$  coordination (similar to  $\text{Ba}_2\text{TiO}_4$ ) or  $^{[5]}\text{Ti}$  (similar to fresnoite glass) (Henderson and Fleet 1995).  
190 Peaks at low wavenumbers ( $\sim 300\text{-}550\text{ cm}^{-1}$ ) also increase in intensity around 10 mol%  $\text{TiO}_2$  and continue  
191 to increase as Ti content increases. At high Ti concentrations, these peaks eclipse the Si-O-Si peaks  
192 observed in the Ti-free glasses. From the similarities with rutile and anatase spectra, these peaks have  
193 been attributed to either  $^{[6]}\text{Ti}$  as a network modifying cation, or  $^{[6]}\text{Ti}$  clusters (Mysen and Neuville 1995).  
194 Based on these observations from previous work, we have qualitatively separated the Raman spectra into  
195 four regions that broadly define the molecular interactions responsible for Raman scattering— “Si” at  
196 high wavenumbers, “Ti low” (low average Ti coordination) through “Ti high” (for Ti in [5]- and [6]-fold  
197 coordination). These assignments are not meant as strict boundaries, but rather as a means to qualitatively  
198 assess changes in the Raman spectra as a function of bulk  $\text{TiO}_2$  content of the glasses. An example of  
199 these peak components is shown in Supplementary Fig. S2.

## 200 **DISCUSSION**

201 The activity of titanium relative to rutile saturation ( $a_{\text{TiO}_2}^{\text{melt-sat.}}$ ) will be calculated in two ways.  
202 The first approach is a rutile-saturation model that relies on the assumption of a constant activity  
203 coefficient,  $\gamma_{\text{TiO}_2}^{\text{melt-sat.}}$ , whereas the second approach will utilize a Ti-in-tridymite thermometer calibrated  
204 in the present study. The structure and chemistry of the glass as a function of bulk  $X_{\text{TiO}_2}$  and partitioning  
205 between the glass and tridymite can help to elucidate which method most accurately records  $a_{\text{TiO}_2}^{\text{melt-sat.}}$ .

### 206 **(1) Rutile saturation approach**

207 The relationship between activity and composition is generally defined as:  $a_{\text{TiO}_2}^{\text{melt}} = \gamma_{\text{TiO}_2}^{\text{melt}} * X_{\text{TiO}_2}^{\text{melt}}$ ,  
208 where  $\gamma_{\text{TiO}_2}^{\text{melt}}$  is the activity coefficient. In an ideal system,  $\gamma_{\text{TiO}_2}^{\text{melt}} = 1$ . In natural magmatic compositions  
209 where rutile saturates at relatively low  $X_{\text{TiO}_2}^{\text{melt}}$ , TiO<sub>2</sub> is assumed to behave within the Henry's Law region  
210 such that  $\gamma_{\text{TiO}_2}^{\text{melt}} \approx k$ , where  $k$  is the Henry's Law constant. In both the ideal and Henry's Law case there  
211 is a linear relationship between  $a_{\text{TiO}_2}^{\text{melt}}$  and  $X_{\text{TiO}_2}^{\text{melt}}$ . Therefore,  $a_{\text{TiO}_2}^{\text{melt}}$  can be calculated by dividing the  
212 measured value by the rutile saturated  $X_{\text{TiO}_2}^{\text{melt}}$  (in an ideal case this value is unity) value:  $a_{\text{TiO}_2}^{\text{ideal}} =$   
213  $\frac{1}{X_{\text{TiO}_2}^{\text{melt}}}$  or  $a_{\text{TiO}_2}^{\text{melt-sat.}} = \frac{X_{\text{TiO}_2}^{\text{melt}}}{X_{\text{TiO}_2}^{\text{melt-sat.}}}$  (Hayden and Watson 2007; Hofmann et al. 2013). Here, we will apply a  
214 similar rutile saturation technique to our experiments in order to estimate  $a_{\text{TiO}_2}^{\text{melt-sat.}}$  (hereafter called  
215  $a_{\text{TiO}_2}^{\text{rut.-sat.}}$ ).

216 To calculate  $a_{\text{TiO}_2}^{\text{melt-sat.}}$  using this technique we established a rutile saturation surface by measuring  
217  $X_{\text{TiO}_2}^{\text{melt}}$  of rutile-saturated NS8 glasses over a range of temperatures. Over a temperature range of 960-1325  
218 °C,  $X_{\text{TiO}_2}^{\text{melt}}$  varied slightly—from ~0.21 to ~0.20 (Fig. 5). Within the standard deviation of the data this  
219 value is effectively a constant, meaning we can treat the rutile-saturated  $X_{\text{TiO}_2}^{\text{melt}}$  value as a constant ~0.21.  
220 We then calculated  $a_{\text{TiO}_2}^{\text{rut.-sat.}}$  using this saturation surface and the linear a-X assumption by dividing  
221  $X_{\text{TiO}_2}^{\text{melt}}$  measured in the rutile-undersaturated glass by  $X_{\text{TiO}_2}^{\text{melt}}$  in the rutile saturated glass at the same  
222 temperature.

## 223 (2) Ti-in-tridymite calibration

224 Rutile-saturated experiments that also contain tridymite were used to calibrate a 1-atm Ti-in-tridymite  
225 thermometer (Fig. 6). The Ti content of tridymite in rutile-saturated experiments was fit to an Arrhenius  
226 relationship with respect to temperature (1/T) by utilizing the same principles as in the Ti-in-quartz  
227 calibration at constant pressure (Wark and Watson 2006), which yields the expression:

228 
$$\ln X_{\text{TiO}_2}^{\text{tridymite}} = \frac{-5299.14}{T (^{\circ}\text{K})} - 0.9242 \quad (2)$$

229 Similar to Wark and Watson (2006) we assume that the Ti solubility in the tridymite follows Henry's  
230 Law behavior such that:

231 
$$a_{\text{TiO}_2}^{\text{Ti-in-tridymite}} = \frac{X_{\text{TiO}_2}^{\text{tridymite}}}{X_{\text{TiO}_2}^{\text{tridymite@sat}}} \quad (3)$$

232 where  $X_{\text{TiO}_2}^{\text{tridymite@sat}}$  is the mol fraction  $\text{TiO}_2$  in tridymite at rutile saturation, at a given temperature.

### 233 **Comparison of $a_{\text{TiO}_2}^{\text{melt-sat.}}$ estimates**

234 If both methods used to calculate  $a_{\text{TiO}_2}^{\text{melt-sat.}}$  in rutile-undersaturated melts agree, they should co-  
235 vary along a line with slope=1. However, the rutile-saturation activity estimates predict  $a_{\text{TiO}_2}^{\text{melt-sat.}}$  in  
236 excess of that from the Ti-in-tridymite estimate (Fig. 7).

237 Changes in the solubility mechanisms of Ti in the melt as a function of bulk Ti content could  
238 result in erroneous estimates of  $a_{\text{TiO}_2}^{\text{rut.-sat.}}$ . Ti coordination changes can be qualitatively assessed using  
239 Raman spectroscopy. Due to the complexity of the Raman spectra and the difficulty of assigning  
240 individual peaks to specific features (e.g., Scannell et al., 2016), Raman spectra were binned into discrete  
241 regions, labelled "Ti high", "Ti med," "Ti low," and "Si," (Fig. 4). Broadly, increasing the Ti content of  
242 the glasses results in changes in Ti coordination and solubility mechanisms in the melt. Although these  
243 assignments are intentionally vague, relative changes to the Raman spectra in these regions as a function  
244 of bulk  $\text{TiO}_2$  correspond to changes in solubility mechanisms for Ti in the melt. These relative changes  
245 are the most important factor for observing if Ti solubility mechanisms change in the glasses as a function  
246 of bulk  $\text{TiO}_2$  content. Several general trends as a function of increasing  $\text{TiO}_2$  can be seen in the Raman  
247 spectra for super-liquidus NS8 glasses. In general, the average coordination of Ti in the melt increases  
248 with decreasing wavenumber. This is consistent with other studies of Ti coordination in  $\text{SiO}_2$ -rich glasses

249 (Chandrasekhar et al. 1980; Henderson and Fleet 1995; Mysen and Neuville 1995; Farges 1997; Reynard  
250 and Webb 1998). In lieu of attempting to curve fit the complex Raman spectra, integrating the area under  
251 the curves over discrete intervals allows us to interpret changes in the average coordination environment  
252 of Ti in the melt as a function of bulk TiO<sub>2</sub> content (Fig. 4, 8). The Raman spectra have been broken into  
253 four regions corresponding to the specific Raman scattering phenomena discussed above. Generally, Ti is  
254 incorporated primarily in [4]-fold coordination at low Ti concentrations (Fig. 8). As more Ti is added to  
255 the system, the average coordination number of Ti increases. At 20 mol% TiO<sub>2</sub>, Ti is primarily  
256 incorporated in [5]- and [6]-fold coordination. The important takeaway from the Raman data is that the  
257 coordination (and subsequent solubility mechanisms governing Ti incorporation into the melt) changes  
258 from almost entirely <sup>[4]</sup>Ti at low concentrations to an average <sup>[5]</sup>Ti or <sup>[6]</sup>Ti higher TiO<sub>2</sub> concentrations.

259         The Raman spectra demonstrate a distinct change in the character of Ti incorporation in the melt  
260 as a function of bulk Ti content. Given that  $\gamma_{TiO_2}^{melt}$  is defined relative to the reactions governing the  
261 solubility of a species in a melt (e.g., Ryerson 1985), the Raman results suggest that the assumption of  
262 constant  $\gamma_{TiO_2}^{melt}$  (akin to the Henry's Law assumptions in natural rutile-undersaturated glasses) is invalid  
263 for the Ti-NS8 system. Departure from Henry's Law behavior can be seen through partitioning of Ti  
264 between tridymite and the melt (Fig. 9). Over a range of temperatures, there is a distinct break in slope of  
265  $D_{TiO_2}^{trd/glass}$  at around 5 mol % TiO<sub>2</sub>. This break also correlates with the rise of the 900 cm<sup>-1</sup> peak in the  
266 Raman spectra. Henderson et al. 2002 and Scannell et al. 2016 also observed that in Ti-bearing Na-  
267 silicate glasses, square pyramidal clusters of [5]-fold Ti start to form around 5 mol % TiO<sub>2</sub>. Similar  
268 changes in coordination have been observed using Raman in other Ti-bearing Na-silicate glasses (e.g.,  
269 Scannell et al. 2016). Combined, these observations are a strong indication that the rutile saturation  
270 model is over-predicting  $a_{TiO_2}^{melt-sat.}$  in our system.

271         Although Raman spectra likely demonstrate that the rutile saturation technique over-predicting  
272  $a_{TiO_2}^{melt-sat.}$  it is worth noting that Ti contents in tridymite can be high (up to 1.75 wt. % TiO<sub>2</sub>). These high

273 concentrations might also be responsible for non-Henrian behavior in the Ti-in-tridymite calibration. For  
274 example, at a given bulk  $\text{TiO}_2$  content  $a_{\text{TiO}_2}^{\text{Ti-in-tridymite}}$  estimates decrease as temperature and the amount  
275 of Ti dissolved in tridymite increase (Fig. 7). Even if these systematic deviations are a demonstration of  
276 departures from Henry's Law behavior, the magnitude of the deviations is significantly less than those of  
277 the rutile saturation model. Further, the Arrhenian behavior of the Ti-in-tridymite calibration (Fig. 6)  
278 where Ti concentrations vary from 0.72-1.75 wt. % suggests that non-Henrian behavior of Ti in tridymite  
279 plays a relatively minor role.

280 A second-order polynomial fit was applied to the two estimates of  $a_{\text{TiO}_2}^{\text{melt-sat.}}$  (Fig. 7). This fit  
281 relates the  $a_{\text{TiO}_2}^{\text{Ti-in-tridymite}}$  ( $a_{\text{TiO}_2}^{\text{melt-sat.}}$  calculated through Ti-in-tridymite) estimates to  $a_{\text{TiO}_2}^{\text{rut.-sat.}}$   
282 ( $a_{\text{TiO}_2}^{\text{melt-sat.}}$  measured using the rutile-saturation method). Because the Ti-in-tridymite estimates are more  
283 likely to predict the actual  $a_{\text{TiO}_2}^{\text{melt-sat.}}$  more accurately, the trend in Fig. 7 is a demonstration of the over-  
284 estimation of  $a_{\text{TiO}_2}^{\text{melt-sat.}}$  using rutile-saturation models relative to  $a_{\text{TiO}_2}^{\text{Ti-in-tridymite}}$  methods. This trend  
285 can then be used to estimate the effect of a variable  $\gamma_{\text{TiO}_2}^{\text{melt}}$  on thermobarometry that utilizes rutile-  
286 saturation models to estimate  $a_{\text{TiO}_2}^{\text{melt-sat.}}$ .

### 287 **Implications for Ti-based trace-element thermobarometry**

288 The high  $X_{\text{TiO}_2}^{\text{melt}}$  required for rutile saturation in the present experiments combined with the  
289 chemical simplicity of the NS8 composition make it difficult to assess whether the analogous over-  
290 estimation of  $a_{\text{TiO}_2}^{\text{melt-sat.}}$  via  $a_{\text{TiO}_2}^{\text{rut.-sat.}}$  will be expected in natural silicate melts where rutile saturation  
291 occurs at significantly lower  $X_{\text{TiO}_2}^{\text{melt}}$  (Hayden and Watson 2007). The interpretation of the Raman  
292 observations indicates that Ti undergoes significant structural changes with variations in  $X_{\text{TiO}_2}^{\text{melt}}$ . At low  
293 concentrations Ti appears to be incorporated as  $^{[4]}\text{Ti}$ , whereas Ti is in a higher average coordination state  
294 ( $^{[5]}\text{Ti}$  or  $^{[6]}\text{Ti}$ ) as rutile saturation in the melt is approached (Fig. 4).

295 The key reason for the inaccuracy of the rutile saturation estimates in our study is changes in the  
296 solubility mechanisms (as inferred by changes in Ti coordination) governing Ti incorporation into the  
297 glass. Although direct comparison with natural composition glasses is not practical at this time, similar  
298 changes in Ti coordination have been observed in natural composition glasses. For example, Farges and  
299 Brown 1997 showed that Ti coordination in rutile-undersaturated glasses shifted from a mixture of [5]-  
300 fold and [6]-fold Ti in basaltic melts to a mixture of [4]-fold and [5]-fold in rhyolitic melts.

301 In order to correct the over-estimation of  $a_{TiO_2}^{melt-sat.}$  via the assumption of constant  $\gamma_{TiO_2}^{melt}$ , we fit a  
302 second-order polynomial forced through the origin to the trend between  $a_{TiO_2}^{Ti-in-tridymite}$  and  $a_{TiO_2}^{rut.-sat.}$   
303 (Fig. 7):

$$304 \quad a_{TiO_2}^{Ti-in-tridymite} = (0.814 * a_{TiO_2}^{rut.-sat.})^2 + 0.174 * a_{TiO_2}^{rut.-sat.} \quad (5)$$

305 Which can be applied in correcting  $a_{TiO_2}^{rut.-sat.}$  estimates of  $a_{TiO_2}^{melt-sat.}$ . Because Ti solubility mechanisms  
306 and changes therein are not precisely known, we fit the data with a second order polynomial primarily  
307 because it was the simplest functional form that best fit the data. Using this fit, if rutile-saturation models  
308 predict  $a_{TiO_2}^{melt-sat.} = 0.5$ , this fit yields a corrected  $a_{TiO_2}^{melt-sat.} = 0.29$ . In natural systems, this correction  
309 for  $a_{TiO_2}^{rut.-sat.}$  could have a significant influence on petrologic interpretations derived from Ti-based trace-  
310 element thermobarometry.

## 311 **IMPLICATIONS**

312 The results of this study indicate that— in the system SiO<sub>2</sub>-TiO<sub>2</sub>-Na<sub>2</sub>O— rutile-saturation  
313 modelling of Ti activity in melts (based on the assumption of a constant  $\gamma_{TiO_2}^{melt-sat.}$ ) can lead to an  
314 overestimate of Ti activity in rutile-undersaturated melts. Changes in the incorporation mechanism for Ti  
315 in the melt are responsible for changes in the  $\gamma_{TiO_2}^{melt-sat.}$  and in turn the overestimation of  $a_{TiO_2}^{melt-sat.}$ .

316 The findings of this study pertain to a chemically simple system that saturates in rutile at ~20  
317 mol% TiO<sub>2</sub> (two orders of magnitude greater than rhyolite melts), and future experimental work on more  
318 natural compositions should be performed to determine whether similar over- or underestimation via  
319  $a_{TiO_2}^{rut.-sat.}$  is observed in natural composition systems. This study lays the groundwork for calculating  
320  $a_{TiO_2}^{melt-sat.}$  using multiple techniques in a single experiment (in this case  $a_{TiO_2}^{rut.-sat.}$  and  $a_{TiO_2}^{Ti-in-tridymite}$ )  
321 as a means to test the validity of assumptions that underlie trace-element thermobarometry. We strongly  
322 caution against using the data presented in this manuscript to interpret natural phenomena until  
323 experiments are performed on more natural bulk compositions.

324 In natural composition glasses (e.g., rhyolites), we were unable to use Raman to resolve potential  
325 changes in Ti coordination in melts as a function of bulk Ti content due to the low concentration of Ti and  
326 subsequently small signal relative to Si in the Raman spectra. Future work using Ti K-edge XANES  
327 (Farges 1997) could help resolve whether the same shifts in Ti solubility mechanisms— and subsequent  
328 deviations from Henrian behavior of Ti in melts— is observed in natural composition magmas.

329 It is difficult if not impossible to perform experiments in a reasonable time frame on quartz- and  
330 zircon-saturated rhyolitic magmas with crystals that are large enough to measure via EPMA. In light of  
331 this, experiments on simple systems like those performed in the present study can provide insight into the  
332 potential behavior of silicic magmas. Despite the limitations of applying Na-silicate composition  
333 experiments directly to natural systems, it is prudent to consider how observations like those made in this  
334 study could potentially affect observations of natural systems. In particular, we will consider the  
335 application to trace-element thermobarometry.

336 Although there is limited data available on coordination of Ti in natural composition glasses, the  
337 data available suggests there are large composition-dependent differences in Ti coordination for differing  
338 glass compositions. For example, (Farges and Brown 1997) demonstrated that basaltic composition  
339 glasses incorporated Ti in various mixtures of <sup>[5]</sup>Ti and <sup>[6]</sup>Ti, whereas rhyolites incorporate Ti in varying

340 proportions of  $^{[4]}\text{Ti}$  and  $^{[5]}\text{Ti}$ . For a given composition, Ti coordination has also been suggested to be a  
341 function of temperature (Lange and Navrotsky 1993). All of these observations are indirectly supported  
342 by differences in Ti solubility in glasses as a function of composition (Hayden and Watson 2007; Gaetani  
343 et al. 2008; Kularatne and Audéat 2014), including a strong increase in Ti solubility in Si-rich peralkaline  
344 relative to peraluminous glasses (Kularatne and Audéat 2014). All of these factors indicate that Ti  
345 solubility in melts and glasses is sensitive to composition and temperature and is incorporated by multiple  
346 substitution mechanisms. The most likely outcome of multiple solubility mechanisms is a change in the  
347  $\gamma_{\text{TiO}_2}^{\text{melt}}$  as a function of  $X_{\text{TiO}_2}^{\text{melt}}$ , which could affect Ti activity estimates utilizing rutile-saturation models.

348 If the results of our study are extended to applications of trace element thermobarometry, the  
349 potential effects of Ti on temperature estimates are significant. Non-Henrian behavior of Ti in melts in  
350 equilibrium with quartz and zircon would result in underestimation of temperatures which rely solely on  
351 rutile-saturation activity models (Fig. 10). These underestimations should not be applied directly to  
352 natural systems but provide an indication of the potential implications of multiple Ti-solubility  
353 mechanisms on Ti activity estimates. Given the amount of Ti required to saturate our experiments in  
354  $\text{TiO}_2$ , the estimates shown in Fig. 10 are likely a worst-case scenario for rutile-saturation estimates. When  
355 possible, applications of Ti-based trace element thermobarometry should be undertaken with multiple  
356 estimates of Ti activity and with care when assessing equilibrium for both melt compositions and mineral-  
357 mineral pairs utilized to determine  $a_{\text{TiO}_2}^{\text{melt-sat.}}$ .

## 358 ACKNOWLEDGMENTS

359 We would like to thank the editorial staff, Calvin Miller and one anonymous reviewer for  
360 comments that aided in the clarity and interpretation of the data presented within this manuscript. We also  
361 thank Dr. Jeff Post for his assistance with XRD measurements. This work was funded by the Carnegie  
362 Postdoctoral Fellowship program.

## 363 REFERENCES



- 364 Armstrong, J.T. (2014) Comparative Performance of SDD-EDS and WDS Detectors for  
365 Quantitative Analysis of Mineral Specimens: The Next Generation Electron Microprobe.  
366 *Microscopy and Microanalysis*, 20, 692–693.
- 367 Bell, R.J., Bird, N.F., and Dean, P. (1968) The vibrational spectra of vitreous silica, germania  
368 and beryllium fluoride. *Journal of Physics C: Solid State Physics*, 1, 299.
- 369 Chandrasekhar, H.R., Chandrasekhar, M., and Manghnani, M.H. (1980) Phonons in TiO<sub>2</sub>-SiO<sub>2</sub>  
370 glasses. *Journal of Non-Crystalline Solids*, 40, 567–575.
- 371 Cody, G.D., Mysen, B.O., and Lee, S.K. (2005) Structure vs. composition: A solid state <sup>1</sup>H and  
372 <sup>29</sup>Si NMR study of quenched glasses along the Na<sub>2</sub>O-SiO<sub>2</sub>-H<sub>2</sub>O join. *Geochim.*  
373 *Cosmochim. Acta*, 69, 2373–2384.
- 374 Farges, F. (1997) Coordination of Ti<sup>4+</sup> in silicate glasses: A high-resolution XANES  
375 spectroscopy study at the Ti K edge. *Amer. Mineral.*, 82, 36–43.
- 376 Farges, F., and Brown, G.E. (1997) Coordination chemistry of titanium (IV) in silicate glasses  
377 and melts: IV. XANES studies of synthetic and natural volcanic glasses and tektites at  
378 ambient temperature and pressure. *Geochimica et Cosmochimica Acta*, 61, 1863–1870.
- 379 Ferry, J.M., and Watson, E.B. (2007) New thermodynamic models and revised calibrations for  
380 the Ti-in-zircon and Zr-in-rutile thermometers. *Contributions to Mineralogy and*  
381 *Petrology*, 154, 429–437.
- 382 Gaetani, G.A., Asimow, P.D., and Stolper, E.M. (2008) A model for rutile saturation in silicate  
383 melts with applications to eclogite partial melting in subduction zones and mantle  
384 plumes. *Earth and Planetary Science Letters*, 272, 720–729.
- 385 Ghiorso, M.S., and Gualda, G.A.R. (2013) A method for estimating the activity of titania in  
386 magmatic liquids from the compositions of coexisting rhombohedral and cubic iron-  
387 titanium oxides. *Contributions to Mineralogy and Petrology*, 165, 73–81.
- 388 Glasser, F.P., and Maar, J. (1979) Phase relations in the system Na<sub>2</sub>O-TiO<sub>2</sub>-SiO<sub>2</sub>. *J. Amer.*  
389 *Ceram. Soc.*, 62, 42–47.
- 390 Hayden, L.A., and Watson, E.B. (2007) Rutile saturation in hydrous siliceous melts and its  
391 bearing on Ti-thermometry of quartz and zircon. *Earth and Planetary Science Letters*,  
392 258, 561–568.
- 393 Henderson, G.S., and Fleet, M.E. (1995) The structure of Ti-silicate glasses by microRaman  
394 spectroscopy. *Can. Mineral.*, 33, 399–408.
- 395 Henderson, G.S., Liu, X., and Fleet, M.E. (2002) A Ti L -edge X-ray absorption study of Ti-  
396 silicate glasses. *Physics and Chemistry of Minerals*, 29, 32–42.

- 397 Hofmann, A.E., Baker, M.B., and Eiler, J.M. (2013) An experimental study of Ti and Zr  
398 partitioning among zircon, rutile, and granitic melt. *Contributions to Mineralogy and*  
399 *Petrology*, 166, 235–253.
- 400 Huang, R., and Audétat, A. (2012) The titanium-in-quartz (TitaniQ) thermobarometer: A critical  
401 examination and re-calibration. *Geochimica et Cosmochimica Acta*, 84, 75–89.
- 402 Johannes, W. (1984) Beginning of melting in the granite system Qz-Or-Ab-An-H<sub>2</sub>O.  
403 *Contributions to Mineralogy and Petrology*, 86, 264–273.
- 404 Kularatne, K., and Audétat, A. (2014) Rutile solubility in hydrous rhyolite melts at 750–900°C  
405 and 2kbar, with application to titanium-in-quartz (TitaniQ) thermobarometry.  
406 *Geochimica et Cosmochimica Acta*, 125, 196–209.
- 407 Lange, R.A., and Navrotsky, A. (1993) Heat capacities of TiO<sub>2</sub>-bearing silicate liquids:  
408 Evidence for anomalous changes in configurational entropy with temperature.  
409 *Geochimica et Cosmochimica Acta*, 57, 3001–3011.
- 410 Le Losq, C., Mysen, B.O., and Cody, G.D. (2015) Water and magmas: insights about the water  
411 solution mechanisms in alkali silicate melts from infrared, Raman, and <sup>29</sup>Si solid-state  
412 NMR spectroscopies. *Progress in Earth and Planetary Science*, 2.
- 413 Maaløe, S., and Wyllie, P.J. (1975) Water content of a granite magma deduced from the  
414 sequence of crystallization determined experimentally with water-undersaturated  
415 conditions. *Contributions to Mineralogy and Petrology*, 52, 175–191.
- 416 McMillan, P. (1984) Structural studies of silicate glasses and melts- applications and limitations  
417 of raman spectroscopy. *American Mineralogist*, 69, 622–644.
- 418 Mcmillan, P., Piriou, B., and Couty, R. (1984) A Raman-Study of Pressure-Densified Vitreous  
419 Silica. *Journal of Chemical Physics*, 81, 4234–4236.
- 420 Mysen, B., and Neuville, D. (1995) Effect of temperature and TiO<sub>2</sub> content on the structure of  
421 Na<sub>2</sub>Si<sub>2</sub>O<sub>5</sub> □ Na<sub>2</sub>Ti<sub>2</sub>O<sub>5</sub> melts and glasses. *Geochimica et Cosmochimica Acta*, 59, 325–  
422 342.
- 423 Mysen, B.O. (2011) Amorphous Materials: An experimental study of phosphorous and  
424 aluminosilicate speciation in and partitioning between aqueous fluids and silicate melts  
425 determined in-situ at high temperature and pressure. *American Mineralogist*, 96, 1636–  
426 1649.
- 427 Mysen, B.O., and Richet, P. (2005) *Silicate glasses and melts: properties and structure*. Elsevier,  
428 Amsterdam; Boston.
- 429 Piwinskii, A.J. (1973) Experimental studies of granitoids from the Central and Southern Coast  
430 Ranges, California. *Tschermaks mineralogische und petrographische Mitteilungen*, 20,  
431 107–130.

- 432 Reynard, B., and Webb, S.L. (1998) High-temperature Raman spectroscopy of Na<sub>2</sub>TiSi<sub>2</sub>O<sub>7</sub>  
433 glass and melt: coordination of Ti<sup>4+</sup> and nature of the configurational changes in the  
434 liquid. *Eur. J. Mineral.*, 10, 49–58.
- 435 Roskosz, M., Mysen, B.O., and Cody, G.D. (2006) Dual speciation of nitrogen in silicate melts  
436 at high pressure and temperature: An experimental study. *Geochimica et Cosmochimica*  
437 *Acta*, 70, 2902–2918.
- 438 Ryerson, F.J. (1985) Oxide solution mechanisms in silicate melts: Systematic variations in the  
439 activity coefficient of SiO<sub>2</sub>. *Geochimica et Cosmochimica Acta*, 49, 637–649.
- 440 Scannell, G., Barra, S., and Huang, L. (2016) Structure and properties of Na<sub>2</sub>O-TiO<sub>2</sub>-SiO<sub>2</sub>  
441 glasses: Role of Na and Ti on modifying the silica network. *Journal of Non-Crystalline*  
442 *Solids*, 448, 52–61.
- 443 Seifert, F., Mysen, B., and Virgo, D. (1983) Raman-Study of Densified Vitreous Silica. *Physics*  
444 *and Chemistry of Glasses*, 24, 141–145.
- 445 Sen, P.N., and Thorpe, M.F. (1977) Phonons in AX<sub>2</sub> glasses: From molecular to band-like  
446 modes. *Physical Review B*, 15, 4030–4038.
- 447 Shane, P., Smith, V.C., and Nairn, I. (2008) Millennial timescale resolution of rhyolite magma  
448 recharge at Tarawera volcano: insights from quartz chemistry and melt inclusions.  
449 *Contributions to Mineralogy and Petrology*, 156, 397–411.
- 450 Thomas, J.B., and Watson, E.B. (2012) Application of the Ti-in-quartz thermobarometer to  
451 rutile-free systems. Reply to: a comment on: ‘TitaniQ under pressure: the effect of  
452 pressure and temperature on the solubility of Ti in quartz’ by Thomas et al. *Contributions*  
453 *to Mineralogy and Petrology*, 164, 369–374.
- 454 Thomas, J.B., Watson, E.B., Spear, F.S., Shemella, P.T., Nayak, S.K., and Lanzirrotti, A. (2010)  
455 TitaniQ under pressure: the effect of pressure and temperature on the solubility of Ti in  
456 quartz. *Contributions to Mineralogy and Petrology*, 160, 743–759.
- 457 Wark, D.A., and Watson, E.B. (2006) TitaniQ: a titanium-in-quartz geothermometer.  
458 *Contributions to Mineralogy and Petrology*, 152, 743–754.
- 459 Wark, D.A., Hildreth, W., Spear, F.S., Cherniak, D.J., and Watson, E.B. (2007) Pre-eruption  
460 recharge of the Bishop magma system. *Geology*, 35, 235–238.
- 461 Watson, E.B., and Harrison, T.M. (2005) Zircon Thermometer Reveals Minimum Melting  
462 Conditions on Earliest Earth. *Science*, 308, 841–844.
- 463 Zotov, N., and Keppler, H. (1998) The influence of water on the structure of hydrous sodium  
464 tetrasilicate glasses. *American Mineralogist*, 83, 823–834.
- 465

466 **TABLES**

467 Table 1: Tridymite compositions Measured by SEM EDS (weight %)

bulk TiO <sub>2</sub>	T (°C)	SiO <sub>2</sub>		TiO <sub>2</sub>		Total
		value	SD	value	SD	
2.5	1225	99.06	0.21	0.13	0.05	99.18
2.5	1250	99.20	0.05	0.12	-	99.33
2.5	1275	99.09	0.14	0.12	0.02	99.21
2.5	1300	99.02	0.23	0.13	0.02	99.15
2.5	1325	98.83	0.15	0.13	0.02	98.96
2.5	1325	98.96	0.22	0.13	0.01	99.09
2.5	1350	99.10	0.24	0.13	0.02	99.23
5	1225	98.60	0.97	0.24	0.03	98.84
5	1250	98.98	0.62	0.32	0.19	99.29
5	1275	99.19	0.23	0.26	0.02	99.45
5	1300	98.99	0.24	0.27	0.02	99.26
5	1325	98.59	0.52	0.28	0.03	98.87
5	1350	98.78	0.40	0.27	0.02	99.05
5	1375	98.57	0.28	0.27	0.03	98.84
5	1400	98.13	0.31	0.28	0.01	98.41
5	1425	98.12	0.21	0.28	0.03	98.40
10	1250	98.48	0.84	0.60	0.04	99.08
10	1275	98.79	0.33	0.59	0.03	99.39
10	1300	98.57	0.33	0.62	0.05	99.19
10	1325	98.59	0.35	0.61	0.06	99.20
10	1350	98.66	0.54	0.64	0.02	99.30
10	1375	98.15	0.62	0.65	0.06	98.80
15	1225	97.39	0.19	1.13	0.08	98.51
15	1250	96.18	3.42	1.11	0.06	97.28
15	1275	97.11	1.55	1.12	0.05	98.23
15	1300	97.84	0.33	1.17	0.05	99.01
15	1325	97.70	0.35	1.19	0.06	98.89
15	1350	97.70	0.67	1.21	0.14	98.91
20	960	97.97	0.38	0.72	0.09	98.70
20	1003	98.06	0.52	0.87	0.06	98.93
20	1010	97.82	0.47	0.74	0.16	98.56
20	1053	98.13	0.08	1.00	0.04	99.13
20	1105	92.04	0.52	1.07	0.06	93.11
20	1128	97.77	0.65	1.17	0.09	98.94
20	1145	95.34	7.81	1.12	0.13	96.45
20	1171	96.79	1.92	1.28	0.19	98.08
20	1185	95.25	0.36	1.52	0.08	96.78
20	1200	97.14	0.87	1.45	0.11	98.59
20	1225	97.78	0.21	1.46	0.05	99.24
20	1251	96.60	1.75	1.59	0.13	98.19
20	1277	97.44	0.42	1.74	0.09	99.18
20	1301	97.11	0.40	1.75	0.05	98.86

468

469 Table 2: Glass Compositions Measured by SEM EDS (weight %)

bulk TiO <sub>2</sub>	T (°C)	Na <sub>2</sub> O		SiO <sub>2</sub>		TiO <sub>2</sub>		Total
		value	SD	value	SD	value	SD	
2.5	1225	11.83	0.15	81.70	0.15	4.96	0.15	98.49
2.5	1250	12.27	0.38	81.62	0.57	4.91	0.10	98.79
2.5	1275	11.81	0.26	82.64	0.24	4.57	0.11	99.02
2.5	1300	11.85	0.44	82.15	0.52	4.62	0.10	98.62
2.5	1325	11.51	0.52	82.38	0.54	4.17	0.05	98.06
2.5	1325	11.26	0.13	83.56	0.17	4.33	0.08	99.15
2.5	1350	11.13	0.13	84.12	0.15	4.23	0.14	99.48
5	1225	9.81	0.78	78.21	0.20	9.63	0.10	97.65
5	1250	9.66	0.51	78.94	0.29	9.34	0.18	97.93
5	1275	9.48	0.32	79.96	0.13	8.86	0.18	98.29
5	1300	9.24	0.19	80.36	0.37	8.63	0.22	98.23
5	1325	9.10	0.16	80.77	0.31	8.43	0.29	98.30
5	1350	8.72	0.05	81.35	0.41	8.01	0.20	98.09
5	1375	8.43	0.12	82.02	0.24	7.61	0.10	98.05
5	1400	7.68	0.20	82.65	0.49	7.10	0.11	97.44
5	1425	7.38	0.11	83.46	0.25	6.71	0.12	97.56
10	1250	8.11	0.32	72.67	0.12	16.16	0.12	96.94
10	1275	7.91	0.17	72.96	0.28	16.15	0.08	97.03
10	1300	7.80	0.19	74.89	0.18	14.67	0.08	97.36
10	1325	8.10	0.08	74.32	0.10	14.86	0.08	97.28
10	1350	7.03	0.18	76.92	0.31	13.71	0.12	97.66
10	1375	6.09	0.25	76.75	0.16	14.29	0.14	97.14
15	1225	8.29	0.31	65.14	0.23	22.44	0.09	95.87
15	1250	8.11	0.21	66.25	0.14	21.57	0.12	95.92
15	1275	7.66	0.08	67.95	0.14	21.08	0.09	96.69
15	1300	6.93	0.19	69.93	0.18	20.02	0.08	96.88
15	1325	6.42	0.08	71.29	0.10	19.07	0.08	96.78
15	1350	6.87	0.26	72.19	0.24	17.89	0.34	96.95
20	960	2.79	0.12	67.46	0.15	24.51	0.19	94.75
20	1003	2.35	0.63	65.70	0.48	24.64	0.77	92.70
20	1010	2.56	0.12	67.02	0.00	25.12	0.26	94.70
20	1053	9.98	2.31	62.35	0.00	23.95	0.04	96.28
20	1105	5.86	0.66	63.30	0.57	24.79	0.22	93.94
20	1128	5.97	0.55	64.18	0.54	25.45	0.37	95.60
20	1145	9.62	0.58	62.55	0.08	24.33	0.12	96.49
20	1171	9.37	0.17	62.36	0.39	24.71	0.12	96.45
20	1185	9.33	0.10	61.82	0.29	24.61	0.12	95.77
20	1200	8.72	0.31	62.91	0.01	24.84	0.06	96.47
20	1225	9.18	0.32	62.80	0.00	24.67	0.03	96.64
20	1251	8.38	3.07	63.31	0.02	24.97	0.09	96.66
20	1277	7.95	0.87	64.05	0.00	24.78	0.05	96.78
20	1301	7.56	0.89	64.89	0.00	24.12	0.03	96.57

470 **FIGURES**

471 Figure 1

472 Upper portion of the  $\text{SiO}_2\text{-Na}_2\text{O-TiO}_2$  phase diagram (Glasser and Maar 1979). Experimental bulk  
473 compositions are represented by black circles. Gray curves are isotherms along the liquidus surface and  
474 solid black lines are liquidus phase boundaries. All experiments except those 20 mol %  $\text{TiO}_2$  were within  
475 the tridymite liquidus phase field.

476 Figure 2

477 Backscatter-electron images of experimental run products that contain (a) tridymite and melt from  
478  $\text{Ti}_{10}\text{NS}_8$  at 1250 °C and (b) tridymite, rutile and melt from  $\text{Ti}_{20}\text{NS}_8$  at 1185 °C.

479 Figure 3

480 Temperature versus melt composition trends for experiments in the bulk composition  $\text{Ti}_5\text{NS}_8$ . These  
481 rutile-undersaturated experiments show a trend of increasing  $\text{TiO}_2$  and  $\text{Na}_2\text{O}$  and decreasing  $\text{SiO}_2$  content  
482 with decreasing temperature as a result of increased down-temperature crystallization of tridymite ( $\text{SiO}_2$ ).

483 Figure 4

484 Raman spectra of quenched glasses from selected bulk compositions from Ti-free ( $\text{NS}_8$ ) to 20 mol %  
485  $\text{TiO}_2$  ( $\text{Ti}_{20}\text{NS}_8$ ). Changes to the Raman spectra with changes in bulk Ti content can be attributed to  
486 changes in the average coordination of Ti in the melt as a function of bulk Ti content. Because peak  
487 assignment in these spectra is not straightforward (e.g., Scannell et al., 2016), spectra were grouped into  
488 regions whose peaks generally represent Si (Si), lower average coordination Ti (“Ti low”), potentially  
489 mixed coordination (“Ti med”), and likely higher average coordination Ti (“Ti high”). Although these  
490 regions are broad and intentionally non-specific, the trends indicate a change in Ti coordination in the  
491 glass as a function of its bulk  $\text{TiO}_2$  content.

492 Figure 5

493 Temperature versus  $X_{\text{TiO}_2}^{\text{melt}}$  for rutile-saturated Ti20NS8 melts. Error bars are  $2\sigma$  standard deviation on  
494 measurements of  $X_{\text{TiO}_2}^{\text{melt}}$ . Over the 341 °C temperature interval,  $X_{\text{TiO}_2}^{\text{melt}}$  varied slightly from 0.2-0.21.  $X_{\text{TiO}_2}^{\text{melt}}$   
495 in rutile-saturated experiments is used to calculate  $a_{\text{TiO}_2}^{\text{rut.-sat.}}$ .

496 Figure 6

497 Ti-in-tridymite calibration from rutile-saturated experiments showing the amount of Ti dissolved in  
498 tridymite ( $\ln X_{\text{TiO}_2}^{\text{tridymite}}$ ) as a function of reciprocal temperature. Red curves are the 95% confidence  
499 bands on the linear regression.

500 Figure 7

501 Comparison of  $a_{\text{TiO}_2}^{\text{Ti-in-tridymite}}$  and  $a_{\text{TiO}_2}^{\text{rut.-sat.}}$  estimates of  $a_{\text{TiO}_2}^{\text{melt-sat.}}$  fitted with a second-order  
502 polynomial forced through the origin. Red curves are the 95% confidence bands. Relative to  
503  $a_{\text{TiO}_2}^{\text{Ti-in-tridymite}}$ ,  $a_{\text{TiO}_2}^{\text{rut.-sat.}}$  consistently over-predicts  $a_{\text{TiO}_2}^{\text{melt-sat.}}$ .

504 Figure 8

505 Areas of regions in the Raman spectra (see Fig. 4) that can be attributed to changes in the structure of Ti  
506 in the melt as a function of TiO<sub>2</sub>. Areas under the background-normalized curves are shown both as the  
507 absolute area as well as relative to the total area. As discussed in the text, these regions are intentionally  
508 broad and reflect general changes in the structure of the melt. In the case of the “Ti high” region, this is  
509 the predominant area in the Ti-free spectrum, and intensity here is due to the symmetrical stretching of Si-  
510 O-Si bonds (Seifert et al. 1983; Mcmillan et al. 1984). As the Ti content of the glasses increased, the  
511 intensity of this region increased from peaks related to Ti in higher average coordination (Mysen and  
512 Neuville 1995), swamping the Si signal from the Ti-free glass. So, whereas the relative area of this region

513 decreased with increasing Ti (b), the absolute area increased with increasing Ti. The + symbols in (b) are  
514 the total area under the curve for the Raman spectra, using the right-side y-axis.

515 Figure 9

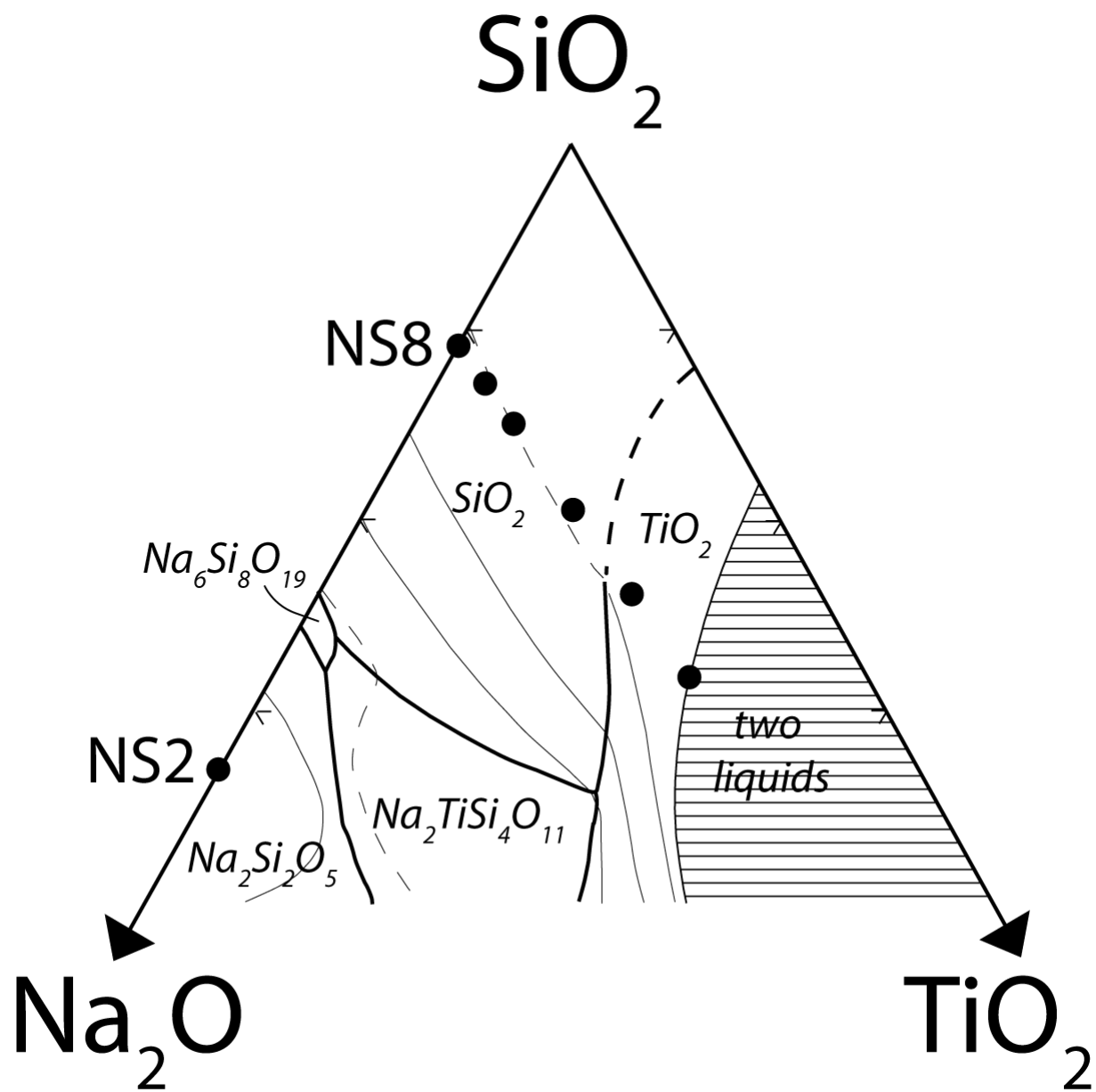
516 Partitioning of titania between tridymite and quenched glasses. At multiple temperatures, changes in bulk  
517 TiO<sub>2</sub> content correlate with changes in the partition coefficient for TiO<sub>2</sub> between tridymite and quenched  
518 glass. The major deviation at ~5 mol% TiO<sub>2</sub> corresponds to a change in the coordination behavior of TiO<sub>2</sub>  
519 in the melt as seen in Raman spectra of the glasses and likely represents a departure from Henrian  
520 behavior of TiO<sub>2</sub> in the glasses.

521 Figure 10:

522 Application of the second-order polynomial fit to the experimental data from this study (equation 5) to  
523 rutile-saturation underestimation of  $a_{TiO_2}^{melt-sat.}$  for Ti-in-quartz and Ti-in-zircon thermobarometry. If  
524 natural magmas behave in a non-Henrian manner as observed in our experiments, rutile-saturation  
525 estimates of  $a_{TiO_2}^{melt-sat.}$  will under-estimate crystallization temperatures. Given that the amount of Ti  
526 required to saturate our experiments in Ti is significantly greater than Ti saturation concentrations in  
527 many natural silicic magmas, the effects observed here are likely a worst-case scenario for rutile-  
528 saturation model estimates.



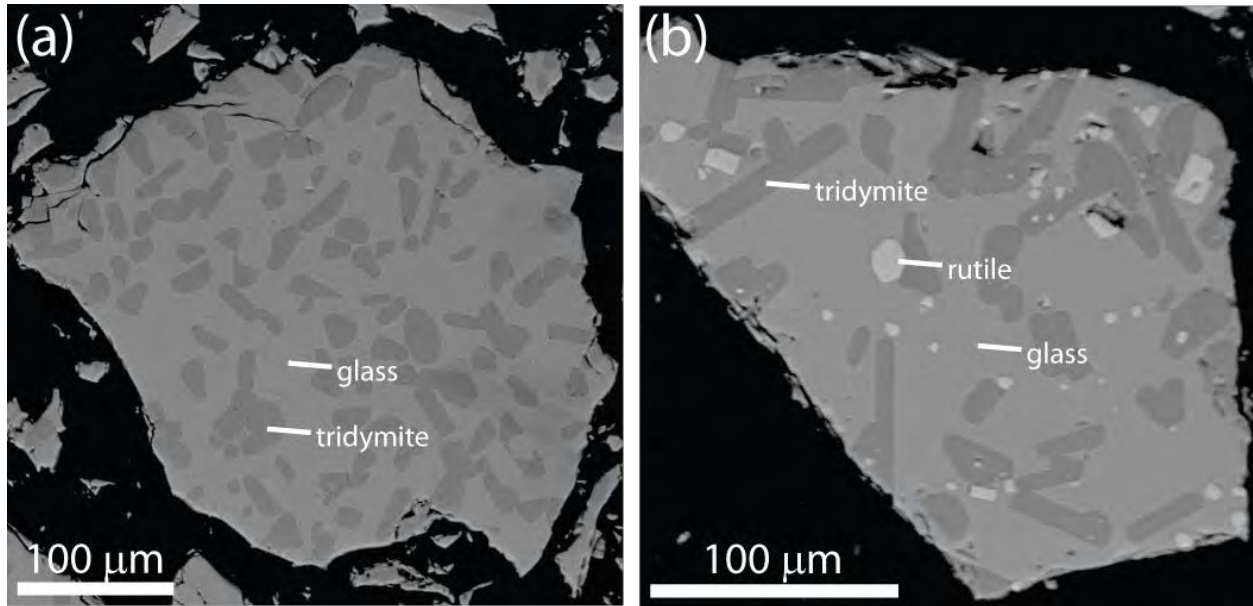
529 Figure 1



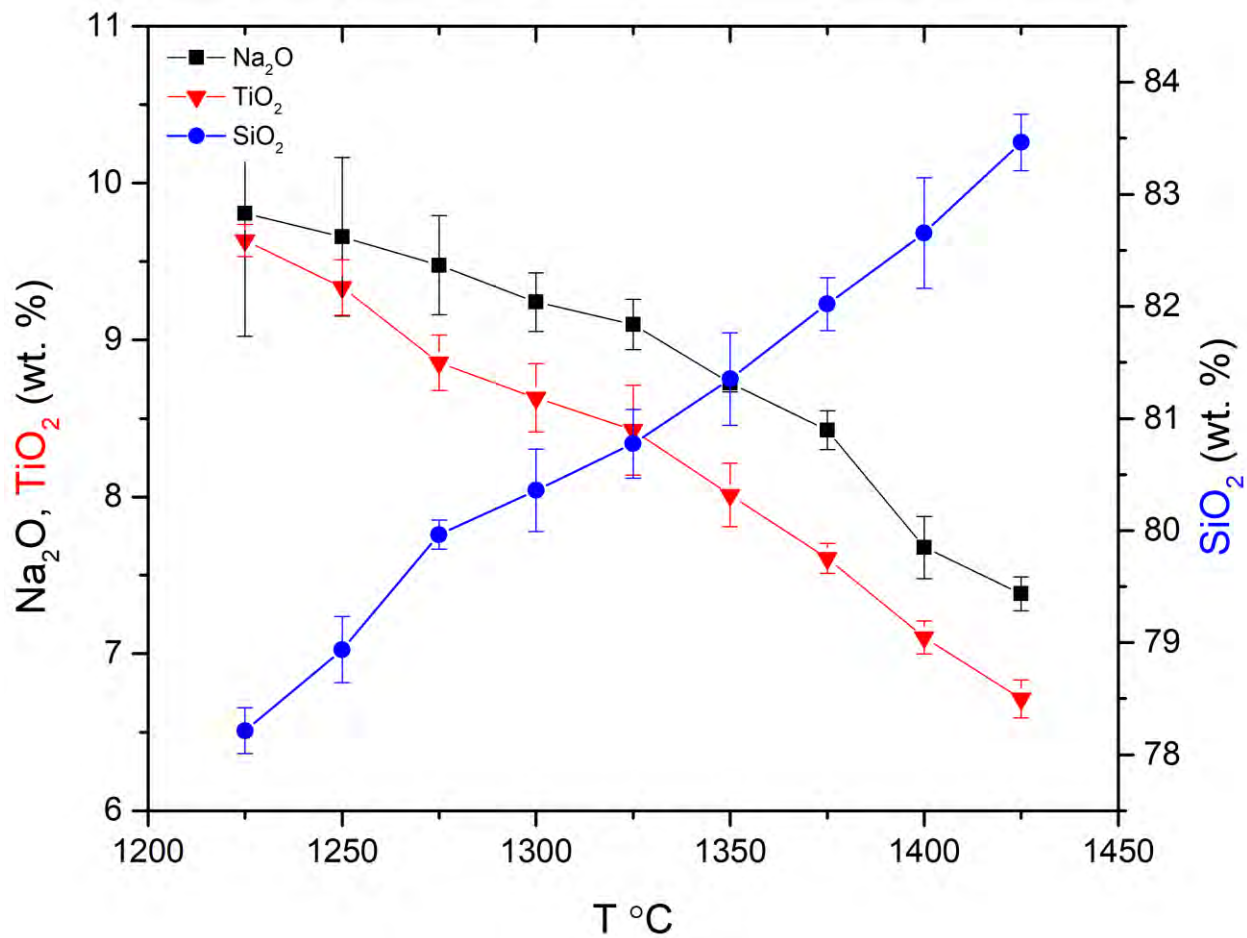
530

531

532 Figure 2

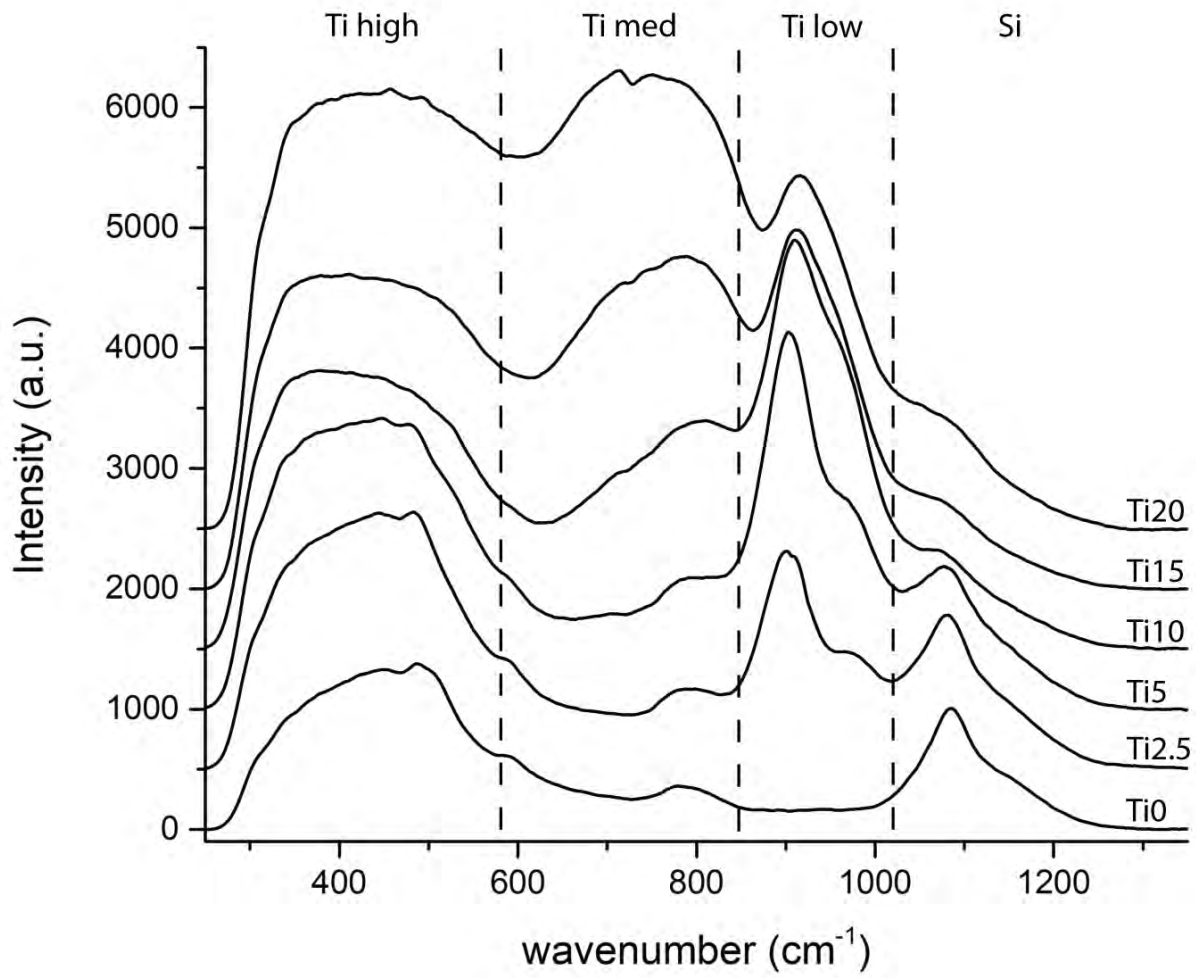


535 Figure 3



536

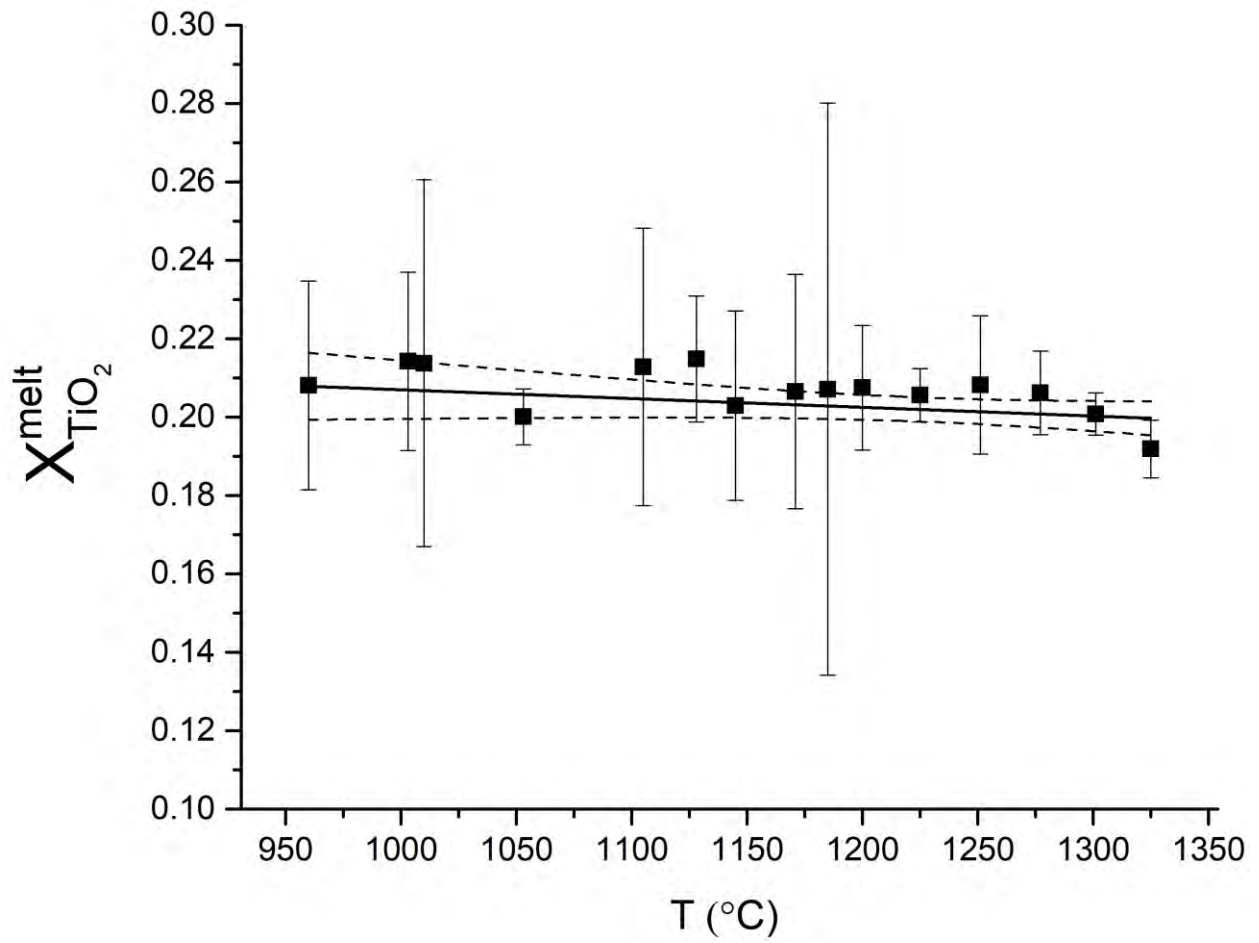
537 Figure 4



538

539

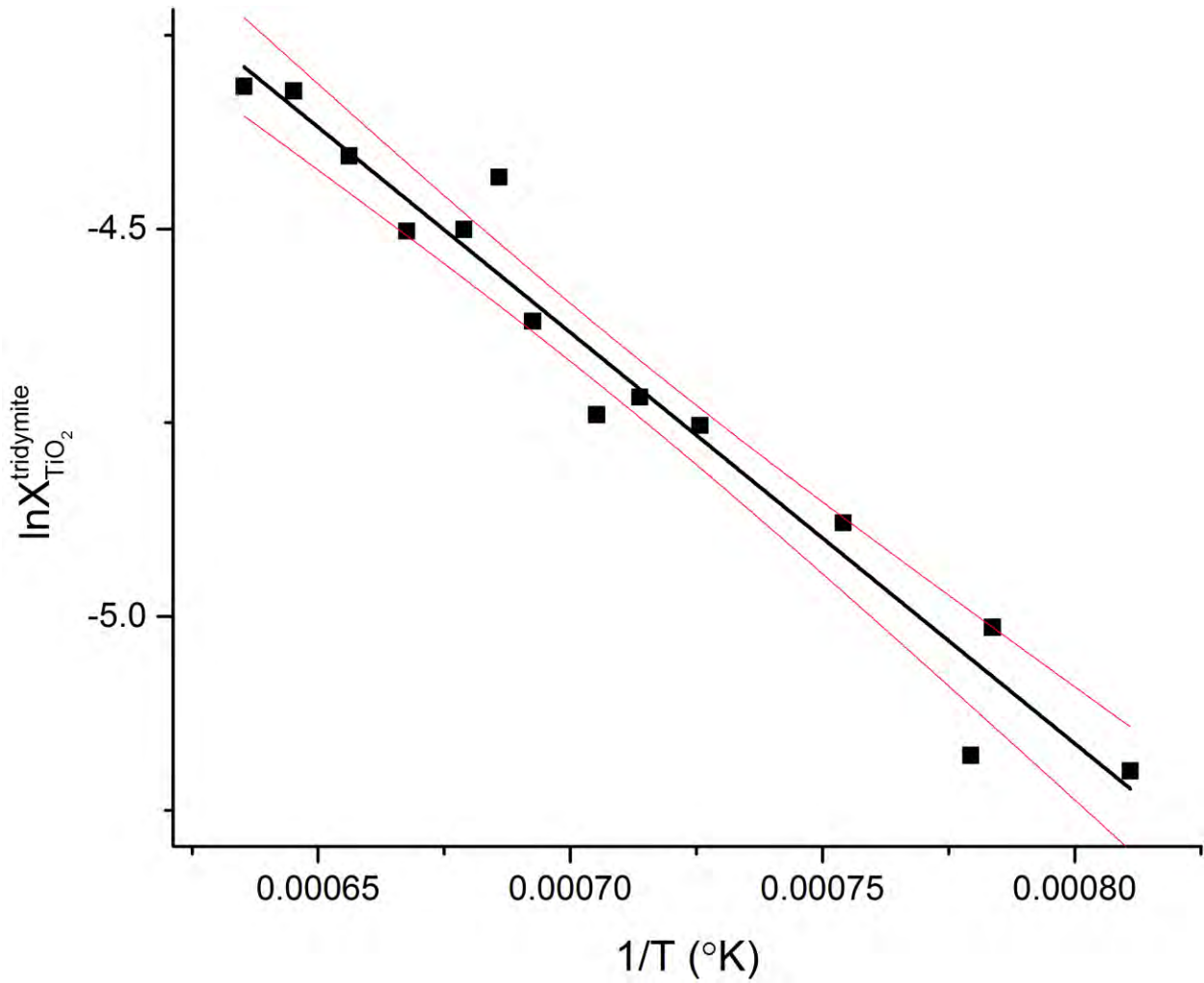
540 Figure 5



541

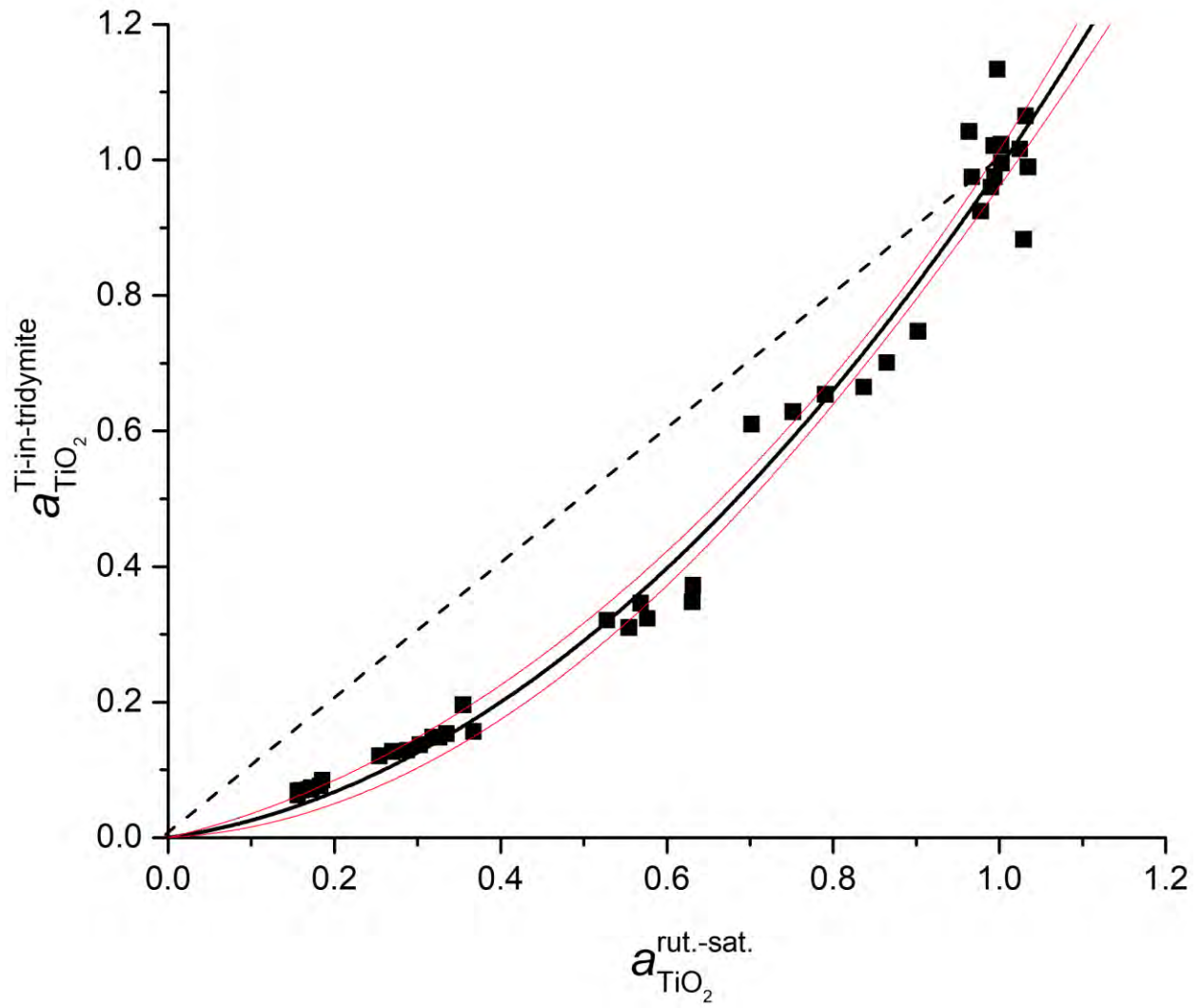
542

543 Figure 6



544

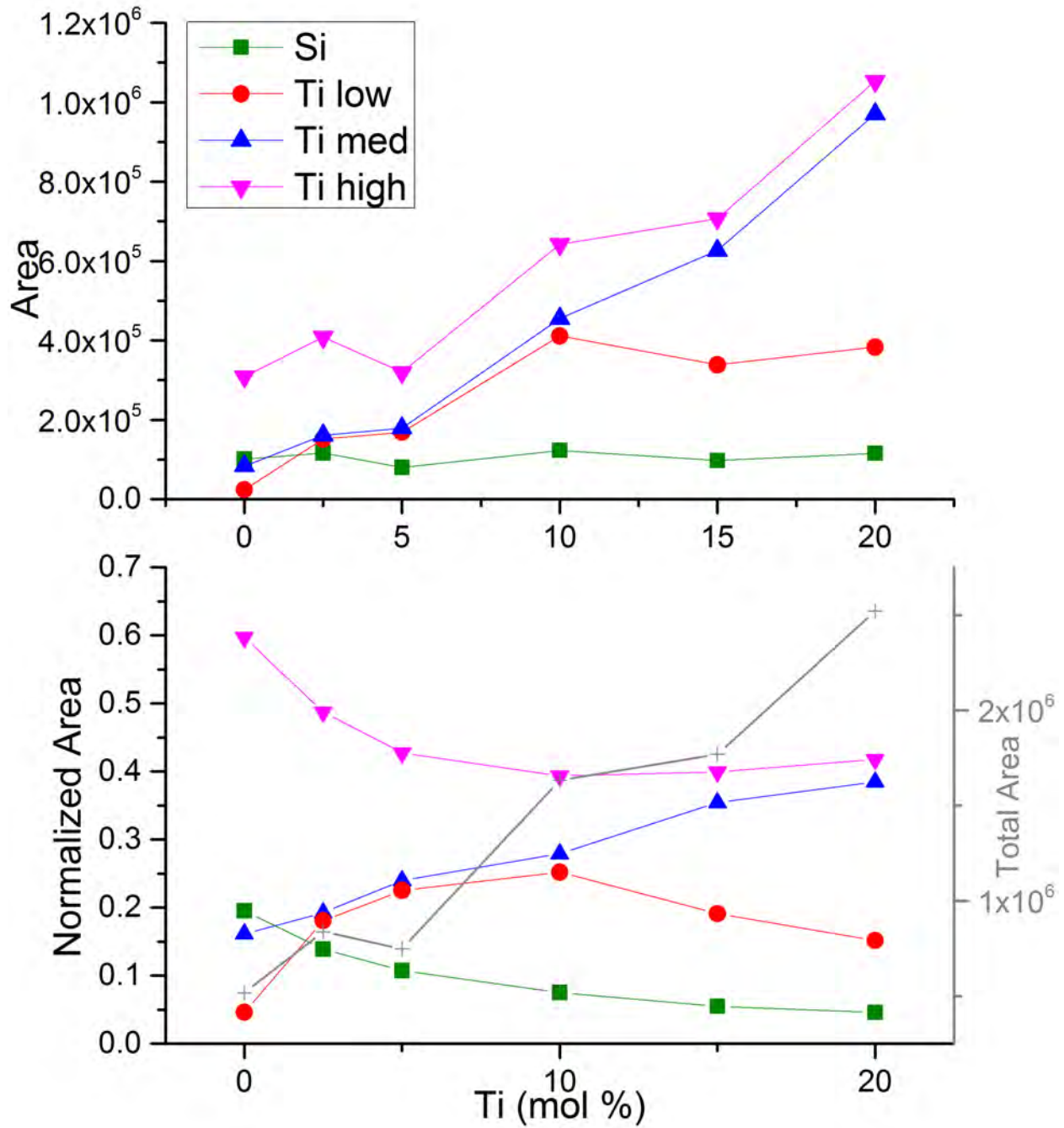
545 Figure 7



546

547

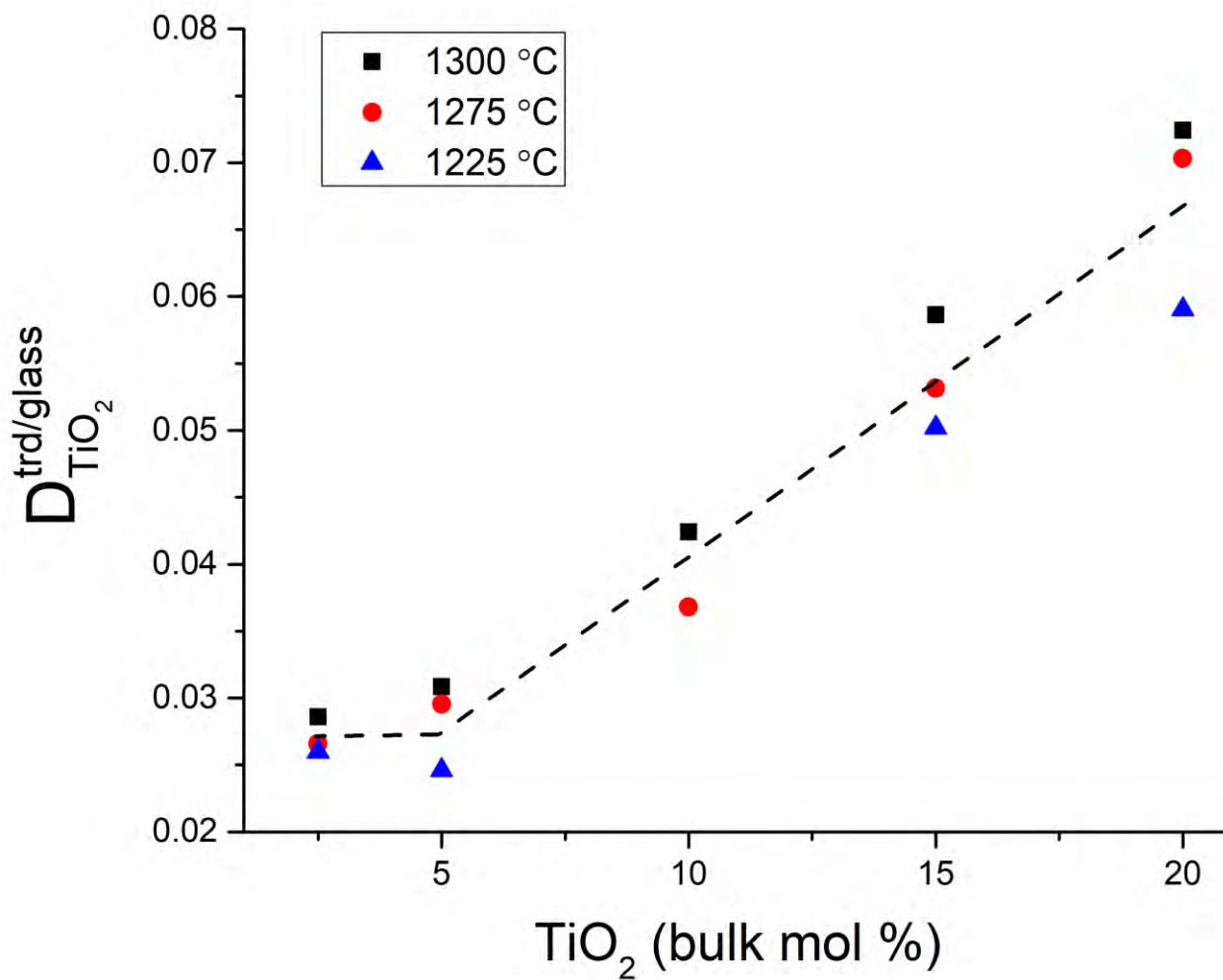
548 Figure 8



549



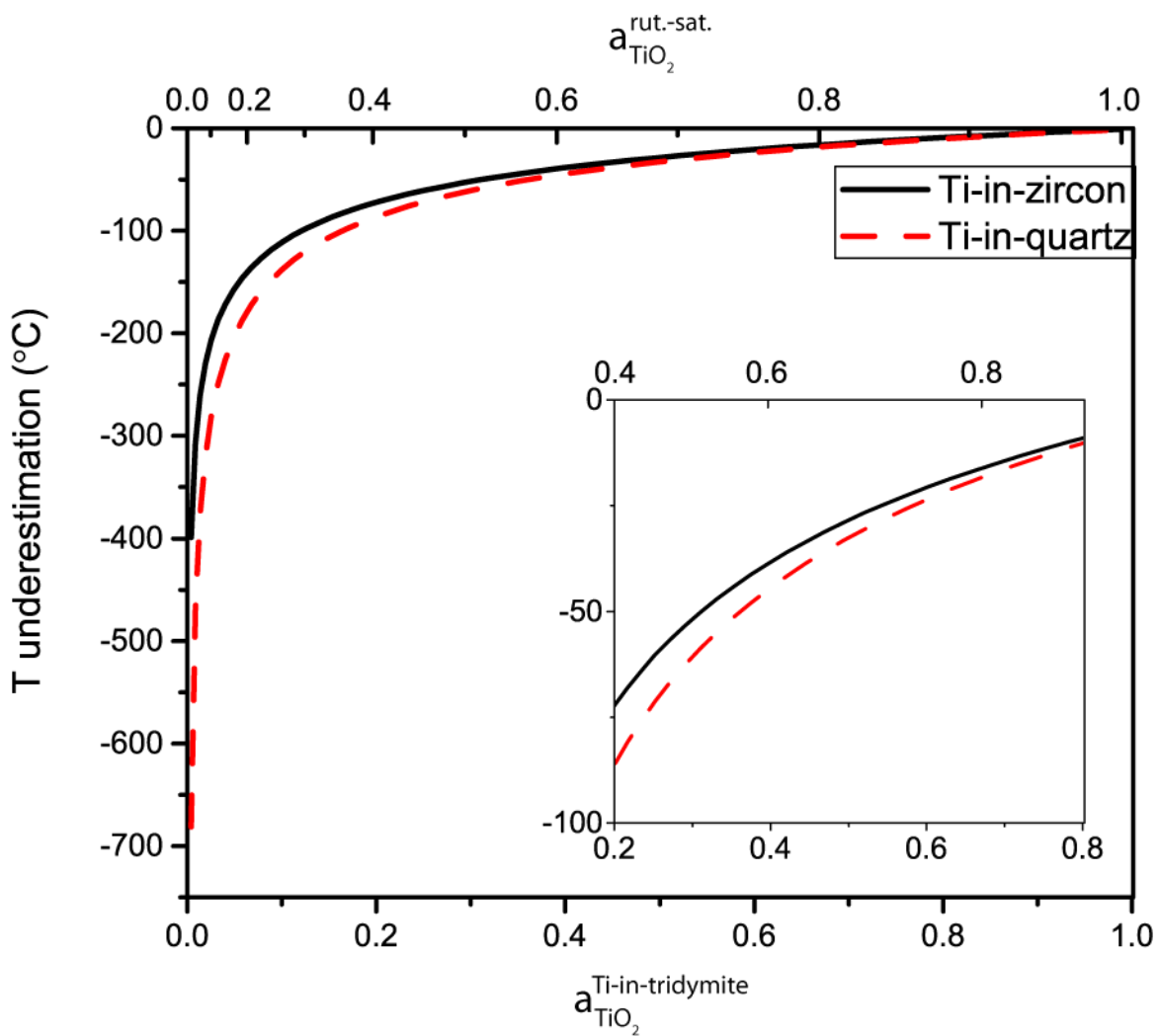
550 Figure 9



551

552

553 Figure 10



554

555